



Swansea University  
Prifysgol Abertawe



## Cronfa - Swansea University Open Access Repository

---

This is an author produced version of a paper published in:

*Journal of Magnetism and Magnetic Materials*

Cronfa URL for this paper:

<http://cronfa.swan.ac.uk/Record/cronfa51634>

---

### Paper:

Nadoum, A., Robinson, F. & Biroasca, S. (2019). On the Correlation between Magnetic Domain and Crystallographic Grain Orientation in Grain Oriented Electrical Steels. *Journal of Magnetism and Magnetic Materials*, 165772

<http://dx.doi.org/10.1016/j.jmmm.2019.165772>

© 2019. This manuscript version is made available under the CC-BY-NC-ND 4.0 license

<http://creativecommons.org/licenses/by-nc-nd/4.0/>

---

This item is brought to you by Swansea University. Any person downloading material is agreeing to abide by the terms of the repository licence. Copies of full text items may be used or reproduced in any format or medium, without prior permission for personal research or study, educational or non-commercial purposes only. The copyright for any work remains with the original author unless otherwise specified. The full-text must not be sold in any format or medium without the formal permission of the copyright holder.

Permission for multiple reproductions should be obtained from the original author.

Authors are personally responsible for adhering to copyright and publisher restrictions when uploading content to the repository.

<http://www.swansea.ac.uk/library/researchsupport/ris-support/>

# On the Correlation between Magnetic Domain and Crystallographic Grain Orientation in Grain Oriented Electrical Steels

A. Nadoum<sup>1</sup>, F. Robinson<sup>2</sup>, S. Biroasca<sup>1</sup>

<sup>1</sup> Materials Research Centre, College of Engineering, Swansea University, Bay Campus, Swansea, SA1 8EN, UK.

<sup>2</sup>Cogent Power, Orb Electrical Steels, Newport, South Wales, NP19 0RB, UK.

## Abstract

The deviation angle of the easy magnetisation  $\langle 001 \rangle$ -axes from the rolling direction (RD) strongly affects the magnetic domain configuration within individual grains and hence the overall magnetic properties in grain oriented electrical steels (GOES). In the current study, both angles of deviations;  $\alpha$ : the angle between  $\langle 001 \rangle$  and in-plane rolling direction, and  $\beta$ : the angle between  $\langle 001 \rangle$  and out-plane rolling direction, were calculated using electron backscatter diffraction (EBSD) raw data to investigate the exact correlation between the crystal orientation and magnetic domain structure. Further, EBSD combined with forescatter detector (FSD) is used to reveal the magnetic domain configuration within individual oriented grains. The microstructure and microtexture of various GOESs with different chemical compositions and magnetic properties were characterised. The magnetic domain patterns were directly imaged and correlated to the crystal orientation and  $\alpha$  and  $\beta$  deviation angles. It is demonstrated that the crystal orientation has a great impact on the magnetic domain patterns, width, and configurations. It was also shown that the grain boundary characteristics have a significant influence on the magnetic domain transfer between neighbouring grains. It was evident that low angle grain boundaries allowed domain transfer without a significant

change in the domain pattern, whereas high angle grain boundaries perturbed the magnetic domain pattern, width, and configuration. Furthermore, it was demonstrated that the size of the deviated orientation grains from ideal (110) <001> GOSS orientation is a critical microtexture parameter for the optimisation of magnetic property. Finally, it is concluded that the magnetic domain patterns and  $\alpha$  and  $\beta$  angle of deviations are strongly correlated to the magnetic losses in GOES.

**Keywords:** EBSD, Forescatter Imaging, GO Electrical Steels, Magnetic Domain.

## **1. Introduction**

### **1.1. Steel Making and GOES Processing**

Grain oriented electrical steel (GOES) is widely used as the core of electric transformers due to its low power losses and good magnetic property [1]. The manufacturing of grain-oriented silicon steel is costly and require careful control of thermomechanical processing in order to generate the desired microstructure and texture for a specific GOES application. In general, GOES production starts from conventional steelmaking, then follows continuous casting, slab reheating at 1400°C, hot rolling to 2mm thickness where the final GOES product inherits its crystallographic texture. A hot band is then annealed at a temperature ranging between 925°C to 1050°C for a very short period before cold rolling [2]. Two-stage cold rolling is followed with intermediate annealing for conventional silicon steels, whereas a single stage of cold rolling is used for high-permeability silicon steels. Following cold rolling, decarburisation, i.e., primary annealing, is performed at 830°C in a wet hydrogen atmosphere after a cold reduction to the final thickness. The last stage of the process is a secondary recrystallisation annealing at 1200°C in a dry protective atmosphere where the

desirable GOSS (110) <110> grains grow and consume other oriented grains. The sharp Goss texture develops owing to abnormal Goss grain growth during the last annealing process [2],[1].

## **1.2 Effect of Microstructure and Crystallographic Texture on Magnetisation**

It is well established that during magnetisation, the rearrangement of the magnetic domain has a significant effect on the magnetic properties in silicon steels, as well as other soft magnetic materials. Thus, direct observation of the magnetic domain alteration allows better understanding of the correlation between core loss and magnetic permeability with the alloy microstructure [3]. Magnetic domains are regions in a magnetic material that are uniformly magnetised or obtained magnetic polarity spontaneously [4]. It is generally accepted that magnetic loss, iron loss, eddy current and hysteresis loss are significantly affected by microstructural characteristics such as microtexture and grain size [5]. Furthermore, it is reported that an abnormal grain growth phenomenon during final high-temperature annealing at the end of the GOES manufacturing process leads to large grains with desired crystal orientation i.e., {110} <001> GOSS texture [6], as shown in Figure 1a. The generation of a strong GOSS texture component contributes chiefly to a reduction in the core power loss in the RD when subjected to a magnetic field [2],[7],[8]. This is critical as the magnetic domain pattern in highly oriented GOES is aligned with the RD. This is also true for 180-degree domain walls that are largely magnetised in the RD. It should be emphasised here that in 180° domains, the magnetic moment changes to the opposite direction i.e., creating strip magnetic domain structure which is found in highly oriented GOSS steel sheet. It was also demonstrated, that the microstructural defects and inclusions can significantly affect the domain wall movement, which results in high magnetic losses [9],[10].

As stated earlier, magnetic property is highly dependant on grain orientation and therefore the deviation of  $\langle 001 \rangle$  crystal axis from RD. There are two main deviation angles that are often considered for easy magnetisation direction, including,  $\alpha$ : an angle between  $\langle 001 \rangle$  axis and the in-plane RD, and  $\beta$ : an angle between  $\langle 001 \rangle$  axis and the out-plane RD, see Figure 1b. These two angles are critical for optimisation of magnetic property. For instance, if an ideal GOSS grain has large  $\alpha$  and  $\beta$  angles, the surface domain closure appears to have  $90^\circ$  which cause a magnetic flux deviation and sub-domain formation that result in minimised magnetostatics energy [11]. It is also reported, that the inclination of  $\beta$  angle is directly proportional to the surface closure domains, [3],[12],[13]. From practical point of view, to reduce surface closure domain and Eddy current losses [14], and hence total power loses in GOES, the sheet thickness is reduced [4],[11],[15]. Note that magnetic flux is referred to the total magnetic field passing through the surface of a steel sheet during the magnetisation process. Also, the magnetostatics energy is referred to the total magnetic charges generated by a magnetic field polariton that leads to the magnetisation of ferromagnets [9].

### **1.3 Magnetic Domain Imaging**

Imaging the domain structure can lead to better understanding of the correlation between microstructural features and magnetic property for optimisation purposes. Many techniques have been utilised to observe magnetic domain structure, sub-structure, movement and mobility during the magnetisation process. These features can be imaged using various techniques and different types of domain viewers used in industry and academia. Conventionally, magnetic powder or magnetic fluids are used with optical microscopy to reveal magnetic domain patterns and flux direction on surface [16]. The advantage of this observation method is that the stray field can be clearly detected. However, the domain

patterns and configuration cannot be directly observed in materials with low stray field or a high magnetic permeability using this method [4]. The magneto-optical or Kerr effect is an alternative technique for domain imaging using standard optical microscopy which can cover large sample area imaging [17], [18]. In general, the magneto-optical effect is based on the rotation of the applied polarised light with resolution limited to that of optical microscopy. Using this method, magnetic domains as narrow as 10 microns in width, can be observed [21]. With the use of periodic photography in magneto-optical microscopy, the domain wall motion can also be observed, which is known as dynamic observation. The limitation of dynamic observation in magneto-optical microscopy even with high-speed photography tools is the low resolution images of domain patterns [4]. A higher resolution is possible with the aid of high-power laser scanning microscopy as reported in [19]. A more sophisticated method is using Transmission Electron Microscopy (TEM) for magnetic domain imaging [20], [21]. In TEM, a relatively low voltage of 100 - 200 keV as well as a high voltage of 1000 keV can be used for such an observation [24]. This allows high-resolution imaging on a nanometre scale and provides high sensitivity for small magnetic patterns alterations. However, the TEM method is limited to a very small observation area and for a thin magnetic material only [22].

Scanning Electron Microscopy (SEM) can assist in providing a better resolution than optical microscopy method for magnetic domain imaging and cover a relatively larger area than TEM method. In SEM condition, the low-energy secondary electrons, which are sensitive to stray field on a magnetised sample surface, are deflected and with the help of detectors that are also very sensitive to electron direction changes, the magnetic domain information can be obtained. It is believed that high energy backscattered electrons emitted as a result of electron striking in SEM, are largely affected by the magnetisation of the sample [4],[23]. In general, there are two types of magnetic contrast that can be obtained using SEM method.

The Type I magnetic contrast can be achieved via secondary electrons to observe the stray field contrast where the sample is oriented perpendicular to the electron beam using 10 KeV or less acceleration voltage during SEM scan. From a large number of these secondary electrons, some are deflected from the sample surface and collected by a highly sensitive detector in the SEM chamber [4]. Type I magnetic contrast is mainly used for hard magnetic materials, whereas Type II magnetic contrast is used for soft magnetic materials, i.e., GOES, that have small stray fields. In Type II contrast, the backscattered electrons are deflected in the forward direction from a tilted sample surface by the local magnetic charge either toward or away from the surface. This creates a difference in contrast for different magnetisation directions in the sample [4],[23]. It is reported that to obtain a maximum magnetic contrast, a 40° tilt angle is considered as an optimum condition [4]. However, in the current study, in order to perform the domain imaging and EBSD simultaneously, a 70°-tilt is applied which provided good magnetic contrast.

By comparing high voltage scanning transmission electron microscopy (STEM) with low voltage SEM method for domain imaging, it was demonstrated in [24] that using 200 keV in STEM can reduce the structural and topography contrasts relative to magnetic signals which assist in providing a clear image with an enhanced magnetic contrast. In the current study careful sample preparation is used to obtain higher magnetic contrast. It is reasonable to assume that SEM magnetic imaging contrast is relatively limited, and post-imaging editing is needed to enhance such a contrast. A technical method of obtaining a high resolution SEM magnetic domain imaging for up to 250 to 300 nm using FSD is reported in [23]. In their study, they used SEM equipped with EBSD detector to image magnetic domains. In general, it is established that during backscatter diffraction imaging method high energy backscattered electrons, ejected from sample surface during SEM scan and this can be affected by the local magnetisation in the sample. Therefore, tilting the sample is needed to

enhance backscattered electrons' deflection by the local domain magnetic charge of the sample. In such a case a large number of electrons are then deflected away from the surface and some are collected by the FSD detectors inside the SEM chamber that are usually positioned on the EBSD phosphor screen's corners. Here the magnetic imaging contrast difference can be observed as different magnetisation polarity.

## **2. Materials and Experimental Procedures**

### **2.1. Material Characterisations**

The materials used in this study were commercial Grain Oriented Electrical Steel (GOES), supplied by Cogent Power in Newport, UK. Seven different GOESs were used with the chemical compositions shown in Table 1. There are small differences between the alloys' chemical compositions. All steel sheets were processed following standard Cogent Power grain oriented electrical steel industrial processing routes. The cast steel underwent slab reheating at 1400°C, and hot rolling to 2mm thickness. A hot band is then annealed at 950°C for a very short period before cold rolling. The decarburisation process, i.e., primary annealing, is performed at 850°C in a wet hydrogen atmosphere. The secondary recrystallisation annealing was conducted at 1200°C in a dry protective atmosphere. As reported in Section 1.1, different rolling passes was employed to produce various thicknesses. The magnetic losses, and permeability B800 (T), of the GOES sheets, were measured at the Cogent Orb Electrical Steel and shown in Table 2. Specimens from each alloy were prepared for SEM characterisations. Samples of fully processed commercial GOES were cut in the RD-TD plane of the steel sheet and mechanically ground and polished to a mirror finished condition. The the samples were then subjected to vibratory polishing for extra 6 hours using a 0.04 µm colloidal silica suspension. For domain imaging,

the specimens were further polished by means of a Hitachi IM-4000 ion beam milling machine. The ion beam milling was conducted following the procedures in [23], and the polishing steps shown in Table 3, to remove surface defects created by mechanical grinding and polishing steps. However, as ion beam milling can also cause some surface damage, thus, further vibrating polishing was carried out using 0.04  $\mu\text{m}$  colloidal silica for extra 4 hours to remove the surface topography created by the ion beam milling. Following sample preparation, SEM and EBSD characterisations were carried out using JEOL FEG SEM 7800F equipped with an Oxford EDS/EBSD systems. During EBSD data acquisition, the samples were tilted to  $70^\circ$  and an acceleration voltage of 20 kV was applied. The working distance was varied between 13 and 17 mm. Furthermore, Oxford Aztec software was used for EBSD and EDS mappings using a variant step sizes depending on the grain size and investigation purposes.

## **2.2 Forescatter Diffraction (FSD) Domain Imaging**

A low voltage Type II condition was applied to visualise the domain patterns and configurations. The magnetic domains were observed using FSD for GOES soft magnetic material. The magnetic contrast was very weak using standard FSD method, thus a relatively high 30kV acceleration voltage was used. Moreover, to increase backscattering coefficient (i.e. the fraction of electrons emerging from the surface), the sample was tilted to  $70^\circ$ . Figure 2 shows certain examples of domain imaging using forescatter detectors under 30 KeV low-voltage SEM conditions. The working distance in the range of 13 - 17mm was used, depending on the obtained magnetic contrast. Figure 2 shows successful imaging examples of magnetic domain pattern and domain transfer between serrated wavy low-angle grain boundary (Figure 2a), high topology non-flat low-angle grain boundary (Figure 2b), domain across small isolated island grain within a large recrystallised grain (Figure 2c),

magnetic domains at triple junction between three different oriented grains with high angle boundaries (Figure 2d). It is evident from Figure 2, that this domain imaging methodology is an effective way of studying domain pattern and configuration as well as its transfer, even without applying external magnetic field. This is vital to observe the original domain structure before the magnetisation process. For instance, Figure 2a shows the domain pattern divergence across the serrated low-angle grain boundary and small precipitates within the grain (see highlighted dashed square). Figure 2b shows the domain fragmentation during its transfer to a different oriented grain through a low angle grain boundary. It should be noted that ion beam milling might have affected the upper grain shown in Figure 2b. As reported in [23], excessive use of ion beam milling can lead to an amorph structure on the surface. Figure 2c shows a lancet narrowly spaced and parallel domain pattern crossing a small island grain without significant diversion. Figure 2d shows a narrow-branched pattern and lancet domain in the top two grains, as well as a very widely spaced domain patterns in the bottom grain which has a different orientation and they are separated by a high grain boundary. As indicated by a small red dashed square on Figure 2d, the branched domain patterns could transfer between the two top grains without significant diversion.

### **2.3 $\alpha$ and $\beta$ Deviation Angles Determination**

To study magnetic properties such as permeability and magnetic losses of GOES, there are two main deviation angles between crystal direction and sample geometry that are often considered. This is critical as the magnetic properties in each individual grain are directly related to its crystallographic alignment with the GOES sample coordinate system. Also, magnetic losses and permeability in GOES are anisotropic physical properties and can be significantly affected by their alignments with the sample coordinate system. As shown in Figure 1b, in the current study, these two angles, namely  $\alpha$  and  $\beta$ , are defined as:  $\alpha$  is the

angle between <001> crystal direction and the in-plane rolling direction (RD) of the GOES sheet, and  $\beta$  is the angle between <001> crystal direction and out-plane rolling plane or Normal Direction (ND). The  $\alpha$  and  $\beta$  deviation angles for each individual grain were calculated using EBSD raw data. From EBSD data, the three Euler angles of individual grain (i.e, crystal coordinate system) and sample geometry (i.e., sample coordinate system) can be obtained in order to calculate the exact values of  $\alpha$  and  $\beta$  angles. First, the EBSD Euler angles were transformed to the orientation matrix using Equation 1 [25]:

$$g(\varphi_1\Phi\varphi_2) = \begin{pmatrix} g_{11} & g_{12} & g_{13} \\ g_{21} & g_{22} & g_{23} \\ g_{31} & g_{32} & g_{33} \end{pmatrix} \dots\dots\dots \text{Eq. 1}$$

The orientation matrix entries are shown as:

$$g(\varphi_1\Phi\varphi_2) = \begin{pmatrix} \cos\varphi_1\cos\varphi_2 - \sin\varphi_1\sin\varphi_2\cos\Phi & \sin\varphi_1\cos\varphi_2 + \cos\varphi_1\sin\varphi_2\cos\Phi & \sin\varphi_2\sin\Phi \\ -\cos\varphi_1\sin\varphi_2 - \sin\varphi_1\cos\varphi_2\cos\Phi & -\sin\varphi_1\sin\varphi_2 - \cos\varphi_1\cos\varphi_2\cos\Phi & \cos\varphi_2\sin\Phi \\ \sin\varphi_1\sin\Phi & -\cos\varphi_1\sin\Phi & \cos\Phi \end{pmatrix} \dots \text{Eq. 2}$$

This orientation matrix assists in the calculation of the deviation angles in relation to specimen coordinate system (X, Y, Z). Here, the crystal direction is denoted as [xyz], where [xyz] corresponds to any direction of interest. Since the crystal direction in coordinate system  $M_{crystal}$  equals  $gM_{speciment}$ , where  $M_{speciment}$  is the specimen direction in the coordinate system [26],[27]. For any crystal direction in [xyz], it can be written as the transpose  $g^tM_{crystal} = M_{speciment}$  as shown in Equation 3, [27].

$$M_{XYZ} = \begin{pmatrix} g_{11} x & g_{21} y & g_{31} z \\ g_{12} x & g_{22} y & g_{23} z \\ g_{13} x & g_{23} y & g_{33} z \end{pmatrix} \dots\dots\dots \text{Eq. 3}$$

The  $\alpha$  and  $\beta$  deviation angles were then calculated following Equations 4 and 5 [27]. Here, only RD direction is considered which is  $\langle 100 \rangle$ , thus  $\langle x'y'z' \rangle$  represent all  $\langle 100 \rangle$  direction. The angles were calculated for all  $\langle 100 \rangle$  symmetrical directions and denoted as  $\langle x'y'z' \rangle$ .

$$\beta_{x'y'z'} = \cos^{-1} \left( \frac{g_{11}x' + g_{21}y' + g_{31}z'}{\sqrt{(g_{11}x' + g_{21}y' + g_{31}z')^2 + (g_{13}x' + g_{23}y' + g_{33}z')^2}} \right) \dots \dots \dots \text{Eq. 4}$$

$$\alpha_{x'y'z'} = \cos^{-1} \left( \frac{g_{11}x' + g_{21}y' + g_{31}z'}{\sqrt{(g_{11}x' + g_{21}y' + g_{31}z')^2 + (g_{12}x' + g_{22}y' + g_{32}z')^2}} \right) \dots \dots \dots \text{Eq. 5}$$

The angle  $\beta_{x'y'z'}$ , is the angle between  $\langle 001 \rangle$  crystal direction and out-plane rolling plane and  $\alpha_{x'y'z'}$  is the angle between  $\langle 001 \rangle$  crystal direction and the in-plane RD of the GOES sheet and both angles are calculated for each of the six directions [27].

### 3. Results and Discussion

Figure 3a shows an electron forward scatter (FS) image for sample A. The Rolling Direction (RD) is closely aligned with specimen Y-Axis as indicated by an arrow in Figure 3. The variations of forward scatter electron intensities in different grains are caused by different local magnetisation polarities, which led to a different contrast in each grain, see Grain 1 (G1) and Grain 2 (G2) in Figure 3. The magnetic domains in Sample A have a simple straight strip pattern in which the strips are transferred from G1 to G2 without perturbation. A magnified area in G1 is shown in Figure 3b. The in-plane angle ( $\alpha$ ) and out-of-plane angle ( $\beta$ ) are calculated for both grains (G1 and G2) and schematically shown in a 2D plane in Figure 3c. There appears a difference between the  $\alpha$  angles measured for the two grains,  $+4.8^\circ$  in G1 and  $+0.85^\circ$  in G2. However, their deviation spread, i.e., range, is in the same direction of parallel to RD, thus the total difference between them is rather small ( $= 3.95^\circ$ ), which reduces the effective deviation from RD. On the other hand, a noticeable difference

is observed between the  $\beta$  angles measured for G1 and G2, with  $+2.8^\circ$  for the former and  $+6.1^\circ$  for the latter. As in  $\alpha$  deviation case, the  $\beta$  angle deviations are aligned with RD in the same direction, i.e., both have (+) values, thus the total difference is also reduced to  $3.3^\circ$ . It appears that this magnitude of deviations did not perturb the striped magnetic domain pattern when crossing the associated grain boundary between the two grains. It has recently been claimed that a grain with a  $\beta$  angle greater than  $0.5^\circ$  showed lancet magnetic domains pattern structure [11],[28]. However, in the current investigation, it appears that G1 and G2 in Sample A did not show any signs of lancet domain structure and they both have  $\beta$  angle values greater than  $0.5^\circ$ , see Figure 3a-c. A possible explanation is that the tensile load parallel to RD applied during thermal flattening, as well as during tension coating at the end of the production line, caused the lancet domain to disappear and the width of the magnetic domain to be reduced. This domain width reduction has some advantages as it is shown to lead to magnetic loss minimisation [12]. Note that the grain boundary angle between G1 and G2 is  $5^\circ$ , which is a low angle grain boundary (LAGB). Furthermore, the Inverse Pole Figures (IPFs) in Figure 3c and Orientation Distribution Functions (ODFs) in Figure 3d showed that both G1 and G2 have a very similar orientation with a strong GOSS texture component intensity. This has assisted the low deviation in ( $\alpha$ ) and ( $\beta$ ) angles between two grains and near coherent strip domain.

Figures 4a and 4b show magnetic domain structures in three neighbouring grains and the domain transfer at a triple junction in Sample B. Figures 4c and 4d, show IPFs and ODFs of the area in Figure 4a, respectively. As shown, G1 with  $+1.6^\circ \beta$  and  $+15.4^\circ \alpha$  has a large slab pattern that is aligned parallel to the G1/G2 grain boundary. The  $\alpha$  angles in G1 and G3, are  $+15.4^\circ$  and  $-6.9^\circ$ , respectively. However, their deviation spread, is in the opposite direction from RD so the total difference between them is very large ( $= 22.3^\circ$ ) and hence increases the effective deviation from RD, significantly. Moreover, there is a slight variation between  $\beta$

angle values for G1 and G3 with values of  $+1.6^\circ$  and  $+2.2^\circ$ , respectively, but aligned with RD, i.e., both have (+) values, thus the total difference is reduced to  $0.6^\circ$ . It appears that this amount of  $\alpha$  angle deviation perturbed the magnetic domain pattern at grain boundaries, although  $\beta$  angle range was negligible.

As highlighted in Figure 4b and indicated by red dashed rectangles, the magnetic domain wall has formed at a  $90^\circ$  angle from the main slab domain structure, which indicates a strong connection to the internal transverse domain. It is widely reported that wide slab-like domains, similar to that for G1 in Figures 4a and b, result in large anomalous eddy-current losses [12][11][29]. Whereas, G3 in Figure 4a, exhibits complex domain patterns are nearly aligned parallel to G3/G1 and G3/G2 grain boundaries receiving magnetic flux from both G1 and G2 grains. Moreover, it seems that the domain structure in G3 is affected by neighbouring grains' magnetic patterns and has  $+2.2^\circ$  ( $\beta$ ) and  $-6.9^\circ$  ( $\alpha$ ) angles. It is evident from Figure 4a, that the magnetic domain structure in G3 does not follow an easy-surface magnetization direction, i.e.,  $\langle 001 \rangle$  in RD, see the G3 3-D crystal in Figure 4. G2, on the other hand, has  $-1.5^\circ$  ( $\beta$ ) and  $+7.25^\circ$  ( $\alpha$ ) angles and shows a complex domain structure with dagger or lancet patterns, which are also known as supplementary magnetic domains. It should be noted that supplementary domains are the sub-domains that appear to reduce magnetostatics' energy, i.e., stray field energy, at the expense of the formation of the additional domain walls. Furthermore, the discontinuation and branching magnetic domain pattern is also observed in G2 and at the G2/G3 grain boundary, see Figure 4a. This might have resulted from the difficulty in transferring the magnetic flux of the same polarity to the neighbouring grains' magnetic domains due to high  $\alpha$  and HAGBs. As shown in Figure 4c, the grain boundary between G1 and G2 is  $13^\circ$ ,  $22^\circ$  between G1 and G3, and  $17^\circ$  between G2 and G3. The ODFs in Figure 4d, show GOSS  $\{110\} \langle 001 \rangle$  texture component deviation

toward  $\{110\} \langle 112 \rangle$ . However, this is expected as G1 has a larger orientation discrepancy with G2 and G3 as shown in the IPFs.

Figure 5a shows a large grain (G1) ( $\sim 752$  microns in diameter) having Cube  $\{100\} \langle 001 \rangle$  orientation in Sample C, see also Figure 5d-e. It is well known that Cube orientation has two easy magnetisation directions [23]. This also applies to G1 due to the fact that it has a small deviation from ideal Cube  $(100) \langle 001 \rangle$  orientation with  $4.8^\circ$  and  $2.4^\circ$   $\beta$  and  $\alpha$  angles, respectively. The FS images in Figures 5a-c show branching magnetic domains pattern perpendicular to RD. See also the highlighted areas by dashed red rectangular shapes in Figures 5a and 5b. This is commonly found in two easy magnetisation directions crystals as stated in [30]. Two specific areas in Figure 5a are magnified for better domain observations; the top side of G1 in the vicinity of the G1/G4 grain boundary is shown in Figure 5b, and lower side of G1 on the G1/G4 boundary in Figure 5c. All the figures demonstrate the domain branching occurrences that is perpendicular to the RD. From Figure 5a, it is clear that G2 is a relatively small grain with a size of 237 microns and shows a wide strip domains' pattern. G2 and G3 have low deviation of  $\beta$  and  $\alpha$  angles. In G3 the magnetic domains exhibit a wide slab pattern, see Figure 5a. Meanwhile, G4 has a  $\beta$  compared to other neighbouring grains where  $\beta$  is equal to  $+6.9^\circ$  and  $\alpha$  equal to  $+0.5^\circ$ . It is clear from Figures 5a-c, that G4 has a complicated magnetic domain pattern that does not follow easy-surface magnetisation direction along RD. The domains major lines in G4 are perpendicular to ( $\perp$ ) RD and nearly parallel to G1 domain patterns, especially in the vicinity of G1/G4 grain boundary, see Figure 5b. Whereas, the magnetic domain in G4 have a complex and fragmented pattern near G1/G4 (bottom side), G4/G3 and G4/G2 grain boundaries, see Figure 5a-c. The magnetic structure in G4 shows signs of a transition-stage magnetic structure. This type of magnetic structure is also reported in [31],[32]. This condition leads to a transition stage where a complex fragmented domain structure and an area of complete rotated patterns toward TD

can exist together within the same grain as clearly can be seen in G4. Moreover, the ODFs in Figure 5d, show strong GOSS in sample C, however, it is not as sharp compared to sample A, see Figure 3d. The IPFs in Figure 5e reveal some orientation difference between G1 and its neighbouring grains. As shown in the figure, G1 is separated from G4 by  $36^\circ$ ; from G2 by  $32.5^\circ$  and from G3 by  $25.8^\circ$ . Whereas, the grain boundary between G2 and G3 is  $8.9^\circ$  LAGB and  $8.2^\circ$  between G2 and G4. Moreover, the grain boundary angle between G3 and G4 is HAGB. It can be concluded that grain boundary has a significant effect on the magnetic domain transfer. For instance, LAGBs allows magnetic pattern continuation and transfer between G2 and G3 with minimum disruption. Whereas, the HAGB could cause large magnetic domain disruption between G1 and G4, see Figure 5a-c.

Table 4 summarise the grain misorientation angle between the identified grains in Samples A, B and C. As shown in Table 4 and Figures 3-5, the grain boundary types are found to be different between Samples A, B and C. It is clear that the grains surrounded by a high angle grain boundary show supplementary magnetic domains and the continuation of these domains to neighbouring grains are disrupted by these boundaries. It was also clear that the magnetic domain is greatly affected by individual grain  $\alpha$  and  $\beta$  deviation angles. Even though much of the literature has shown that the higher deviation  $\beta$  angles result in complex structure pattern, however, this was not observed in the current study. For instance, Sample A with a higher than  $0.5^\circ$   $\beta$  deviation shows no sign of a supplementary domain structure.

For better understanding of the effect of  $\alpha$  and  $\beta$  deviation angles on magnetic performance, over 15 grains in each of the 7 samples with different thickness were analysed using EBSD row data. In the current study, the Gaussian Distribution Function for  $\alpha$  and  $\beta$  angles is calculated for each individual grain in all the samples and shown in Figure 6. As shown in Figures 6a and 6b, Sample A has the smallest range distribution (narrowest peak) for both

$\alpha$  and  $\beta$  angles, while sample B has the largest range distribution (widest peak) for both angles. Moreover, Sample D has a smallest average deviation ( $\sim 0$ ) for angle  $\beta$  and sample E has a small average deviation ( $\sim 0$ ) for angle  $\alpha$ . Further comparison between the samples was rather difficult using this method, thus, a new data representation method was used in this study in order to visualise the deviation angles in correlation with the magnetic performance in each sample. This new data visualisation method is clarified in Figure 7, where sample F used as an example. A Gaussian distribution curve is plotted, where the average ( $\mu$ ) is the centre of the curve. Statistically, the majority of data have  $\pm 1$  standard deviation of the Gaussian curve, that is 68% of the data lies between  $\pm 1$  range ( $-\sigma$  to  $\sigma$ ) from the average ( $\mu$ ). The standard deviation denoted by ( $\sigma$ ). The average ( $\mu$ ) was calculated using Equation 6 [33]:

$$\mu = \frac{1}{n} \sum_{i=1}^n x_i \quad \dots\dots\dots \text{Eq. 6}$$

where  $x_i$  are the deviation angles and ( $n$ ) is the total number of the angle values. The standard deviation is calculated using Equation 7:

$$\sigma = \sqrt{\frac{\sum_{i=1}^n (x_i - \mu)^2}{n-1}} \quad \dots\dots\dots \text{Eq.7}$$

The standard deviation calculation of 68% of the data was then subtracted from the average for the lower limit of the range. As for the upper limit of the range, the standard deviation is added to the average, as shown in Equations 8 and 9, respectively:

$$\text{The lower limit of the range} = \mu - \sigma \quad \dots\dots\dots \text{Eq.8}$$

The upper limit of the range =  $\mu + \sigma$  ..... Eq.9

Plotting the range from Eq.8 to Eq. 9 (lower to the upper limit) range results in the 68% of the distribution range of the angular deviation, which is another representation of the Gaussian curve. By plotting 68% angular deviation distribution, the samples can be compared in terms of deviation angles versus magnetic losses and B800 values. Figure 8 shows the scatter plots of deviation angles of all the grains for each sample using equations 6 and 7. This data representation was assisted in the range determination of the  $\alpha$  and  $\beta$  angles and directly correlated the angles spreads between all the samples. For instance, Sample B has a very large angles spread which reduced its magnetic performance, whereas, Sample A has a lowest range and exhibited a good magnetic performance.

The plots of  $\alpha$  and  $\beta$  angular distributions as functions of magnetic losses and B800 values are shown in Figure 9 and Figure 10, respectively. It should be noted that the sample thickness is provided in the legend as a prefix to each sample. In general, Figure 9a shows the  $\beta$  angle distribution correlation with overall magnetic loss; the smaller  $\beta$  distribution range results in lower magnetic losses. Figure 8b demonstrates similar behaviour of the effect of  $\alpha$  deviation on magnetic losses. As shown in Figures 9 and 10, sample A has the smallest deviation spread, for both  $\beta$  and  $\alpha$  angles, which resulted in the lowest magnetic losses and the highest B800 value. Although  $\beta$  value in Sample A is not as close to a zero value as the other samples, it has a very limited spread from the average value, as well as smaller distribution range in both deviation angles. Similarly, sample D, has very low magnetic losses and a high B800 value. Although  $\beta$  and  $\alpha$  angles deviation in Sample D is close to the zero value, however, they have a wider spread compared to Sample A, which might explain the relatively higher magnetic losses and lower B800 in Sample D as shown in Figures 9, 10 and Table 2. Furthermore, as can be seen in Figure 9, Sample E has a

relatively small range distribution as well as near-zero angular deviation spread. The magnetic losses in Sample E which has a 0.27 mm in thickness, is low (0.92 W/kg Value) compared to the 0.23 mm thickness sample D. From Figure 9, the deviation angles distribution effects on the magnetic losses can be seen, and it is evidence that a small distribution in angular deviation results in lower magnetic losses. However, there is some irregularity. For instance, sample C has a relatively high magnetic loss (1.11 W/kg) although it has a low  $\alpha$  and  $\beta$  deviation angle distribution ranges, see Figure 9. Thus, the magnetic performance can be affected by other factors such as grain size and chemical composition. For example, the relatively large grains in Sample C increased the Eddy current losses and this is in an agreement with [34]. Moreover, Aluminium (Al) and Nitrogen (N) which forms the main primary grain growth inhibitor (AlN) are not present in sample C. This resulted in low permeability and high magnetic losses in Sample C. As for Samples B and G, the large spread of deviation angels has caused a high magnetic loss and a low permeability. Sample B has higher losses due to the fact that it has a thicker cross-section (0.27 mm) compared to sample G (0.23 mm). Note that sample B has wider distribution ranges in both  $\beta$  and  $\alpha$  angles than those of Sample G which also affects the magnetic losses, see Figure 9. Moreover, comparing Samples G and B to sample F, the effect of sample thickness can clearly be clearly. For instance, Sample F (0.35 mm) has smaller  $\alpha$  and  $\beta$  distribution ranges than those of Sample G (0.23 mm) and C (0.23 mm), but it has poor magnetic performance that can be directly linked to its thickness. As reported in [14] the larger sheet thickness, the higher Eddy current losses in the sample.

Figure 10 shows the distribution of angular deviation from the average values of  $\alpha$  and  $\beta$  angles versus the B800 value for all the 7 samples investigated in this study. It can be seen that samples with the lowest spread in the deviation angle  $\alpha$  have the highest B800 values. As an example, see Sample A which has B800 of 1.94 T. It is widely reported that the

deviation angle  $\alpha$  is directly correlated to permeability [35]. This is in an agreement with the finding in the current study. For instance, the samples with the highest permeability, i.e., sample A, has the highest B800 value with the lowest distribution of deviation angles  $\alpha$  and  $\beta$ ; followed by Sample E (0.27 mm), then Sample D (0.23 mm). Although Sample D has lower  $\beta$  angle distribution range than in sample E, it has lower B800 1.92 T compared 1.93 T. This is directly related to the  $\alpha$  angel distribution which is directly correlated to permeability performance since sample E has a very low  $\alpha$  range. As for the samples with low B800 values, sample C with 1.86 T performed better than samples B, G and F (1.85 T, 1.84 T and 1.83 T, respectively). The sample thickness effects on the permeability is evident in Figure 10. For instance, although sample F (0.35 mm thickness) has much lower  $\alpha$  and  $\beta$  distribution rage than that for samples G and B, but it has the lowest B800 value. This demonstrates the high impact of sample thickness on both B800 values and magnetic losses. Moreover, sample G has a high distribution range of both deviation angles with a thickness of 0.23 mm, which is thinner than sample B (0.27 mm), yet it has a lower B800 value. Although both samples B and E have a thickness of 0.27mm, sample E magnetic performance was much higher due to the minimum deviation angles. The effect of thickness on magnetic performance can be also magnified by reducing the deviation angles as the case of sample E, where sample E magnetic performance is higher compared to most of other 0.23mm samples due to a smaller range of deviation angles. This trend discrepancy required further investigation in order to understand Sample G's low B800 value as well as Sample C's high magnetic losses, which will be discussed in the next section.

The effect of grain size on magnetic losses was investigated using a SOKEN tester to measure magnetic losses on two different samples with different grain size distributions. A region in Sample G was characterised for this purpose. As shown in Figure 11a, this region contained relatively small grain sizes. The grain orientation deviation from ideal GOSS

orientation is shown in Figure 11b. Figure 11d shows an overall strong Goss texture of the sample. The grain G1 in figure 11b have the highest deviation from ideal Goss orientation ( $> 20^\circ$ ) in the maps, whereas G2, G3 and G4 deviate by  $15^\circ$ - $17^\circ$  from GOSS orientation and they are surrounded by grains with the smallest deviation from GOSS orientation ( $< 5^\circ$ ). The IPFs and grain boundary misorientation angle maps are shown in Figure 11c. Apparently, only a few grains have LAGB ( $< 10^\circ$ ) and the majority of the grain boundaries are HAGBs ( $> 10^\circ$ ). It seems that the small gain size and HAGBs were the reasons for the increase in magnetic losses 1.13 W/kg at 1.7 T in this particular region.

Figure 12a shows a relatively large grain in sample D. Form the magnetic measurement data it was clear that this particular area in sample D has a lower magnetic loss of 0.77 W/kg at 1.77 T compared to the area investigated in Sample G. Due to the large grain sizes, sample D was cut into a few smaller sections for EBSD acquisitions. It is clear from Figure 12a, that G1 is mostly surrounded by LAGBs ( $5^\circ < \text{Misorientation angle} < 20^\circ$ ) and only a few segments of HAGBs  $> 20^\circ$ . G1 is neighbour with G2 and G3 that have GOSS orientations, see Figure 12b. Small grains with high deviation from ideal GOSS orientation were found on G1/G2 and G1/G3 grain boundaries in this region of sample D, see Figure 12b. However, their very small sizes provide little barrier to magnetic flux to encounter the neighbouring grains where the large grain boundary area fraction facilitate the flux transfer between the large grains. Therefore, these small grains have negligible effects on overall magnetic losses. Comparing the 2 observed areas in Samples G and D, see Figures 11d and 12c, it can be seen that the region with relatively large grain in Sample D has a sharper GOSS texture than the area with relatively small grain in Sample G. Hence, the grain size of the ideal GOSS orientation (110)  $\langle 001 \rangle$  have a great effect on magnetic losses and permeability.

In summary, the results showed that the grain size, grain boundary,  $\alpha$  and  $\beta$  deviation angles and sample thickness have a great influence on magnetic properties in GOES. It was found that low deviation and distribution of  $\alpha$  and  $\beta$  results in high permeability and low magnetic losses. It was also shown that deviation angles have a high impact on magnetic domain pattern, where the high deviation in  $\alpha$  and  $\beta$  results in complex magnetic structure. Hence, it can be concluded that flat strip magnetic domain configuration results in good magnetic performance in terms of magnetic losses and permeability. In general, the areas with low angle grain boundaries showed low magnetic losses. In contrast, the samples with high angle grain boundaries showed high magnetic losses. Furthermore, the sample thickness found to have a great impact on magnetic losses and permeability. It was demonstrated that the sample thickness has played a more influential factor than  $\alpha$  and  $\beta$  deviation angle spreads in magnetic losses of the sample.

#### **4. Conclusions**

In the present study, magnetic domain structure and pattern in grain-oriented silicon steel are imaged and correlated to the deviation angles  $\alpha$  and  $\beta$ ; in-plane and out-of-plane deviation angle from  $\langle RD \rangle$ , respectively. The effects of  $\alpha$  and  $\beta$  angle deviations, sheet thickness, grain size, crystallographic grain orientation and grain boundary misorientation on magnetic domain structure and magnetic performance were thoroughly investigated with the main conclusions are summarised below:

1. FDS method is proved to be a powerful technique to reveal magnetic domains in GOES with clearer domain visualisation than other conventional optical and Kerr microscopy tools. The advantage of this method is that no additional equipment was needed to reveal the magnetic patterns in the SEM system. The limitation of FSD magnetic imaging is the

surface finishing, as an ion beam miller can affect the magnetic structure by amorphizing the surface lattice.

2. The deviation angles; in-plane angle ( $\alpha$ ) and out-of-plane angle ( $\beta$ ) have a great influence on the magnetic domain patterns as well as the magnetic property of GOES. The higher the  $\alpha$  and  $\beta$  deviation angles, the lower permeability and higher magnetic losses. It was demonstrated that  $\alpha$  angle deviation has more effects on the permeability than  $\beta$  angle deviation range, whereas  $\beta$  angle has more influence on magnetic losses.

3. The magnetic domain pattern continuation and transfer between the neighbouring grains are largely affected by the grain boundary misorientation angle. It was demonstrated that the magnetic domain patterns can easily be transferred across the grains through LAGB. Whereas the magnetic domain pattern was distorted and transformed into a complex structure when encountered grain with HAGB.

4. It is concluded that the sample thickness and grain size are more influential factors than  $\alpha$  and  $\beta$  deviation angles for magnetic property optimisation. However, the magnetic performance can be improved by reducing the deviation angles in thick GOSS sheets.

## References

[1] Liu, Hai-Tao, Sheng-Jie Yao, Yu Sun, Fei Gao, Hong-Yu Song, Guo-Huai Liu, Lei Li, Dian-Qiao Geng, Zhen-Yu Liu, and Guo-Dong Wang, "Evolution of microstructure, texture and inhibitor along the processing route for grain-oriented electrical steels using strip casting," *Mater. Charact.*, vol. 106, pp. 273–282, 2015.

- [2] T. Kubota, M. Fujikura, and Y. Ushigami, "Recent progress and future trend on grain-oriented silicon steel," *J. Magn. Magn. Mater.*, vol. 215, pp. 69–73, 2000.
- [3] J. W. Shilling and G. L. Houze, "Magnetic Properties and Domain Structure in Grain-Oriented 3% Si-Fe," *IEEE Trans. Magn.*, vol. 10, no. 2, pp. 195–223, 1974.
- [4] A. Hubert and R. Schäfer, *Magnetic domains: the analysis of magnetic microstructures*, 3rd ed. New York: Springer Science & Business Media, 2008.
- [5] A. A. Almeida, D. Rodrigues-Jr, L. Perassa, J. Leicht, and F. Landgraf, "Anomalous Loss Hysteresis Loop," *Mater. Res.*, vol. 17, no. 2, pp. 494–497, 2014.
- [6] D. Dorner, S. Zaefferer, L. Lahn, and D. Raabe, "Overview of Microstructure and Microtexture Development in Grain-oriented Silicon Steel," *J. Magn. Magn. Mater.*, vol. 304, no. 2, pp. 183–186, 2006.
- [7] C. Gheorghies and A. Doniga, "Evolution of Texture in Grain Oriented Silicon Steels," *J. Iron Steel Res. Int.*, vol. 16, no. 4, pp. 78–83, 2009.
- [8] M. Matsuo, "Review Texture Control in the Production of Grain Oriented Silicon Steels Grain Oriented Silicon Steels Texture Control for Improved Magnetic Properties," *IS// Int.*, vol. 29, no. IO, pp. 809–827, 1989.
- [9] Y. Ushigami, M. Mizokami, M. Fujikura, T. Kubota, H. Fujii, and K. Murakami, "Recent development of low-loss grain-oriented silicon steel," *J. Magn. Magn. Mater.*, vol. 254–255, pp. 307–314, 2003.
- [10] N. Takahashi, Y. Suga, and H. Kobayashi, "Recent developments in grain-oriented silicon-steel," *J. Magn. Magn. Mater.*, vol. 160, pp. 98–101, 1996.
- [11] T. Nozawa, M. Mizogami, H. Mogi, and Y. Matsuo, "Magnetic properties and dynamic domain behavior in grain-oriented 3 % Si-Fe," *IEEE Trans. Magn.*, vol. 32, no. 2, pp. 572–589, 1996.
- [12] M. Imamura and T. Sasaki, "The status of domain theory for an investigation of magnetostriction and magnetization processes in grain-oriented si-fe sheets," *Phys. Scr.*,

vol. 1988, no. T24, pp. 29–35, 1988.

[13] M. Imamura, S. Tadashi, and A. Saito, “Magnetization Process and Magnetostriction of a 4% Si-Fe single crystal close to (110)[001],” *Ieee*, vol. 17, no. 5, pp. 2479–2485, 1981.

[14] Z. Xia, Y. Kang, and Q. Wang, “Developments in the production of grain-oriented electrical steel,” *J. Magn. Magn. Mater.*, vol. 320, no. 23, pp. 3229–3233, 2008.

[15] S. Chikazumi and C. D. Graham, *Physics of Ferromagnetism 2e*, vol. 94. Oxford University Press on Demand, 2009.

[16] F. Bitter, “Experiments on the nature of ferromagnetism,” *Phys. Rev.*, vol. 41, no. 4, pp. 507–515, 1932.

[17] C. A. Fowler Jr and E. M. Fryer, “Magnetic domains on silicon iron by the longitudinal Kerr effect,” *Physical Review*, vol. 86, no. 3. p. 426, 1952.

[18] H. J. Williams, F. G. Foster, and E. A. Wood, “Observation of magnetic domains by the Kerr effect,” *Phys. Rev.*, vol. 82, no. 1, p. 119, 1951.

[19] C. D. Wright, W. W. Clegg, A. Boudjemline, and N. A. E. Heyes, “Scanning Laser Microscopy of Magneto-Optic Storage Media,” *Jpn. J. Appl. Phys.*, vol. 33, no. 4R, pp. 2058–2065, 1994.

[20] H. W. Fuller and M. E. Hale, “Determination of magnetization distribution in thin films using electron microscopy,” *J. Appl. Phys.*, vol. 31, no. 2, pp. 238–248, 1960.

[21] M. E. Hale, H. W. Fuller, and H. Rubinstein, “Magnetic Domain Observations by Electron Microscopy,” *J. Appl. Phys.*, vol. 30, no. 5, pp. 789–791, 1959.

[22] Y. Zhao, G. C. Wang, and T. M. Lu, “Experimental methods in the physical sciences,” *Charact. Amorph. Cryst. Rough Surf. Princ. Appl.*, 2001.

[23] M. Gallagher, N. Brodusch, R. Gauvin, and R. R. Chromik, “Magnetic domain structure and crystallographic orientation of electrical steels revealed by a forescatter detector and electron backscatter diffraction,” *Ultramicroscopy*, vol. 142, pp. 40–49, 2014.

[24] T. Yamamoto, H. Nishizawa, and K. Tsuno, “High voltage scanning electron

microscopy for observing magnetic domains,” *J. Phys. D. Appl. Phys.*, vol. 8, no. 9, pp. 18–21, 1975.

[25] H.-J. BUNGE, *Texture analysis in materials science: mathematical methods*. London: Butterworth-Heinemann, 1982.

[26] V. Randle and O. Engler, *Introduction to Texture analysis: Macrotecture, Microtexture & Orientation Mapping*. Amsterdam: Gordon and Breach Science Publishers, 2000.

[27] N. Bernier, E. Leunis, C. Furtado, T. Van De Putte, and G. Ban, “EBSD study of angular deviations from the Goss component in grain-oriented electrical steels,” *Micron*, vol. 54–55, pp. 43–51, 2013.

[28] W. S. Paxton and T. G. Nilan, “Domain configurations and crystallographic orientation in grain-oriented silicon steel,” *J. Appl. Phys.*, vol. 26, no. 8, pp. 994–1000, 1955.

[29] S. Shin, R. Schafer, and B. C. De Cooman, “Grain boundary penetration by lancet domains in Fe-3%Si grain-oriented steel,” *IEEE Trans. Magn.*, vol. 46, no. 9, pp. 3574–3581, 2010.

[30] A. N. Bogdanov, *Magnetic Domains. The Analysis of Magnetic Microstructures*, vol. 25, no. 2. Springer Science & Business Media, 1999.

[31] L. J. Dijkstra and U. M. Martius, “Domain pattern in silicon-iron under stress,” *Rev. Mod. Phys.*, vol. 25, no. 1, pp. 146–150, 1953.

[32] O. Perevertov and R. Schäfer, “Magnetic properties and magnetic domain structure of grainoriented Fe-3%Si steel under compression,” *Mater. Res. Express*, vol. 3, no. 9, pp. 1–12, 2016.

[33] R. Peck, C. Olsen, and J. L. Devore, *Introduction to statistics and data analysis*. Boston: Cengage Learning, 2015.

[34] C. M. B. Bacaltchuk, G. A. Castello-Branco, H. Garmestani, and A. D. Rollett, “Effect of magnetic field during secondary annealing on texture and microstructure of nonoriented silicon steel,” *Mater. Manuf. Process.*, vol. 19, no. 4, pp. 611–617, 2004.

[35] M. McCarty, G. L. Houze, and F. A. Malagari, "Texture-Electrical-Property Correlations in Oriented Silicon Steel," *J. Appl. Phys.*, vol. 38, no. 3, pp. 1096–1098, 1967.

**Table captions:**

**Table 1:** Chemical compositions in wt.% of fully processed commercial (GOSS)s used.

**Table 2:** Magnetic performance of the commercial GOES sheets, showing magnetic losses (W/Kg) and permeability B800 (T).

**Table 3:** Ion beam polishing steps using Hitachi IM-400 tool.

**Table 4:** Grain boundary angles and types in Samples A, B and C.

**Figure Captions:**

**Figure 1:** Schematics showing ideal GOSS orientation (a) and definitions of  $\alpha$  and  $\beta$  angles:  $\alpha$  is the angle between  $\langle 001 \rangle$  and in-plan RD and  $\beta$  is the angle between  $\langle 001 \rangle$  and out-plan RD (b).

**Figure 2:** Magnetic domain imaging using FSD, (a) Magnetic domain transfer through a serrated low angle grain boundary and precipitates, showing strip branching indicated by dashed white lines, (b) Ion beam milling effects on domain fragmentation depending on grain orientation, (c) Magnetic domain transfer through a small island grain, (d) Lancet domains configuration in the top grains and large slab magnetic domain configuration in the bottom grain.

**Figure 3:** (a) FSD image of magnetic domain in Sample A, revealing strip magnetic pattern transfer between G1 and G2, (b) high magnified area in G1, (c) IPF//RD and IPF//ND maps, grain boundary and ( $\alpha$  and  $\beta$ ) deviation angles are shown on the images, (d)  $\phi_2 = 0^\circ$  and  $\phi_2 = 45^\circ$  ODF sections for the map in (c) showing strong GOSS.

**Figure 4:** (a) Magnetic domain at triple junction in sample B: Slab magnetic pattern in G1, Lancet magnetic pattern in G2 and Complex magnetic pattern in G3, (b) A magnified magnetic image showing  $90^\circ$  domain wall in the same area in (A) indicated by dashed red rectangular shape, (c) IPF//RD and IPF//ND maps, grain boundary and ( $\alpha$  and  $\beta$ ) deviation angles are shown on the images, (d)  $\phi_2 = 0^\circ$  and  $\phi_2 = 45^\circ$  ODF sections for the map in (c) showing strong GOSS.

**Figure 5:** (a) FSD image of magnetic domain in Sample C, G1 with Cubic orientation  $\{100\} \langle 001 \rangle$  showing magnetic pattern branching perpendicular to RD indicated by by red dash squares, large slab magnetic pattern in G2 and G3 and complex magnetic pattern in G4, (b) Magnified area of G1 showing magnetic stirp pattern branching, (c) Complex magnetic pattern in G4, (d)  $\phi_2 = 0^\circ$  and  $\phi_2 = 45^\circ$  ODF sections for the map in (e) showing strong GOSS. (e) IPF//RD and IPF//ND maps, grain boundary and ( $\alpha$  and  $\beta$ ) deviation angles are shown on the images,

**Figure 6:** Gaussian Distribution Functions for deviation angles (a)  $\alpha$ , (b)  $\beta$ , for all 7 samples A-G.

**Figure 7:** An example of Gaussian Distribution Function calculated for sample G; 68% of the data acquired between  $-\mu$  and  $\mu$ , ( $\sigma$ ) is the average value.

**Figure 8:** A scatter plot showing the deviation angles of all the grains in each sample plot.

**Figure 9:** Sample magnetic losses versus (a)  $\beta$  deviation angle distribution (b)  $\alpha$  deviation angle distribution, for all the 7 samples A-G, the sample's thickness shown in the legend.

**Figure 10:** Sample B800 (T) versus (a)  $\beta$  deviation angle distribution (b)  $\alpha$  deviation angle distribution, for all the 7 samples A-G, the sample's thickness shown in the legend.

**Figure 11:** (a) A region in Sample G with a relatively small grain microstructure, (b) GOSS orientation deviation map ( $0^\circ$  to  $20^\circ$  deviation from ideal GOSS), (c) IPF//RD and IPF//ND maps for the area in (A), grain boundary and ( $\alpha$  and  $\beta$ ) deviation angles are shown on the images, (d)  $\phi_2 = 0^\circ$  and  $\phi_2 = 45^\circ$  ODF sections for the map in (c) showing strong GOSS.

**Figure 12:** (a) A region in Sample D with large grain microstructure, a large grain with strong GOSS orientation and grain boundaries are shown (b) GOSS orientation deviation maps for two areas, (c)  $\phi_2 = 0^\circ$  and  $\phi_2 = 45^\circ$  ODF sections for the map in (a) showing strong GOSS.

Sample	Si	C	N	Mn	P	Al	Cu	Ni	Cr	Sn	Pb
A	3.32	0.0017	0.0011	0.089	0.025	<0.005	0.006	<0.005	0.12	0.052	0.002
B	3.11	0.0026	<0.001	0.058	0.001	<0.005	0.12	0.062	0.028	0.013	<0.001
C	3.33	0.0022	-	0.069	0.009	-	0.098	0.005	0.024	0.01	0.004
D	3.19	0.0025	<0.001	0.067	0.009	<0.005	0.063	0.031	0.052	0.11	0.003
E	3.19	0.0018	<0.001	0.065	0.009	<0.005	0.073	0.036	0.064	0.12	0.003
F	2.84	0.0016	<0.001	0.049	0.011	<0.005	0.15	0.057	0.26	0.018	0.003
G	3.23	0.0038	<0.001	0.059	0.003	<0.005	0.16	0.078	0.046	0.014	<0.001

Table 1: Chemical compositions in wt.% of fully processed commercial (GOSS)s used.

Sample	Magnetic losses (W/kg)	B800 (T)	Thickness (mm)
A	0.82	1.94	0.23
B	1.17	1.85	0.27
C	1.11	1.86	0.23
D	0.88	1.92	0.23
E	0.92	1.93	0.27
F	1.4	1.83	0.35
G	1.09	1.84	0.23

Table 2: Magnetic performance of the commercial GOES sheets, showing magnetic losses (W/Kg) and permeability B800 (T).

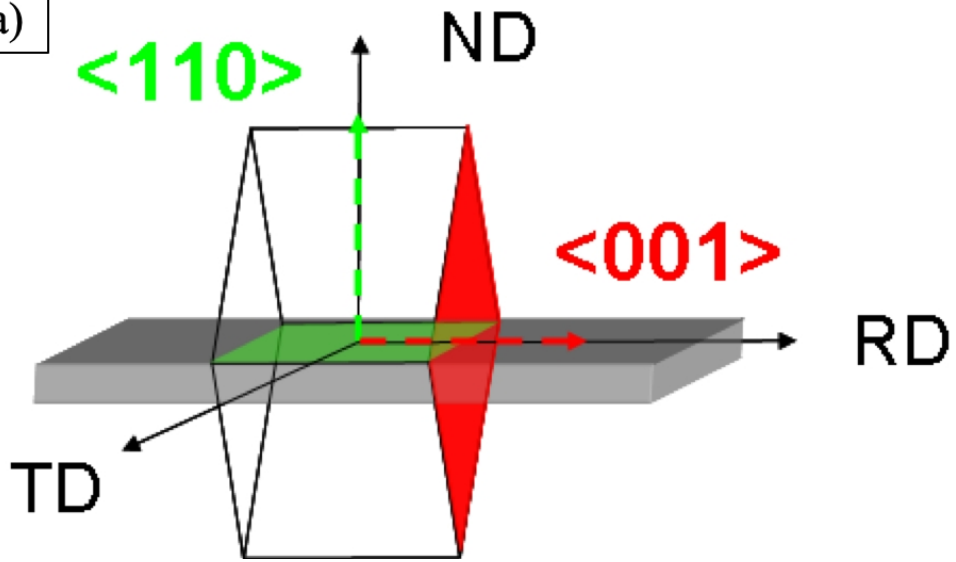
Voltage (keV)	Angle of Incidence (°)	Time (min)
6	10	30
4	10	60
2	8	120

Table 3: Ion beam polishing steps using Hitachi IM-400 tool.

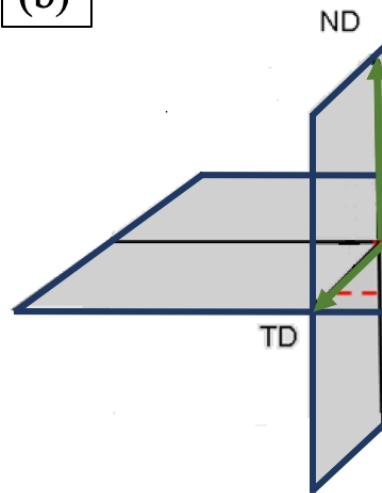
Grains	Grain Boundary Type	Misorientation Angle (°)
<b>Sample A</b>		
<b>G1-G2</b>	LAGB	5.0°
<b>Sample B</b>		
<b>G1-G2</b>	HAGB	13.0°
<b>G1-G3</b>	HAGB	22.0°
<b>G2-G3</b>	HAGB	17.0°
<b>Sample C</b>		
<b>G1-G2</b>	HAGB	32.5°
<b>G1-G3</b>	HAGB	25.8°
<b>G1-G4</b>	HAGB	36.0°
<b>G2-G3</b>	LAGB	8.9°
<b>G2-G4</b>	LAGB	8.2°
<b>G3-G4</b>	LAGB	11.3°

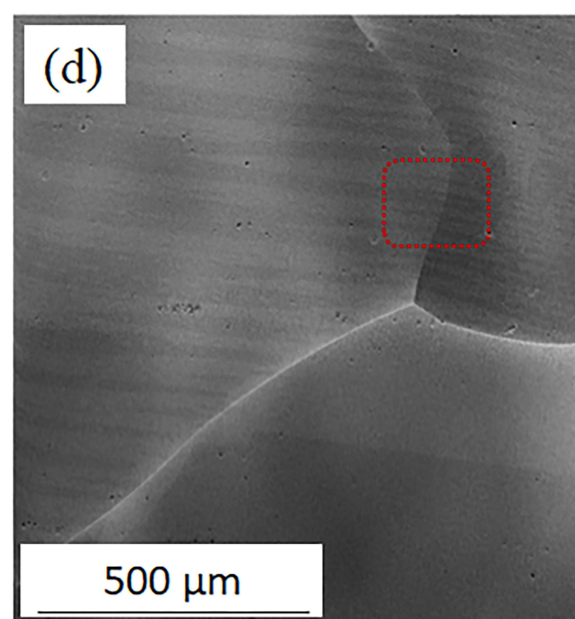
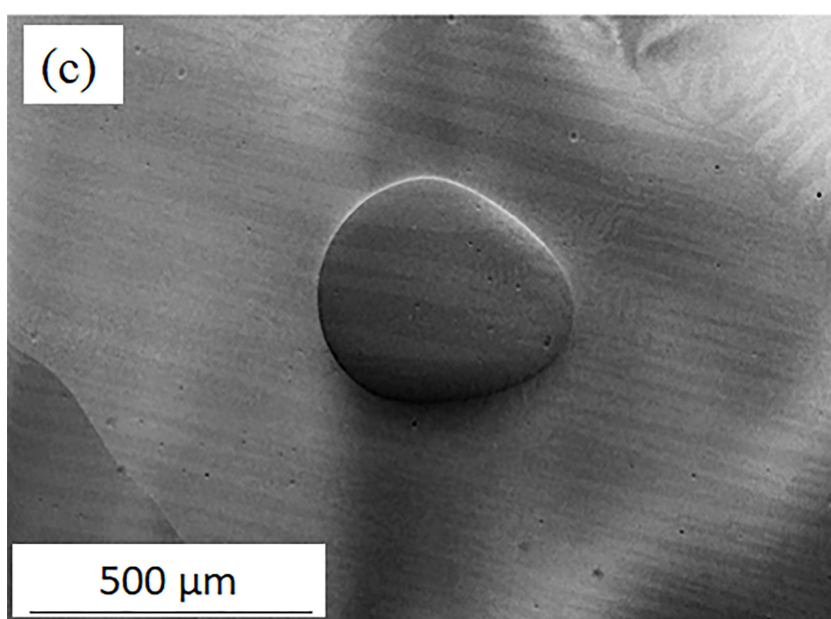
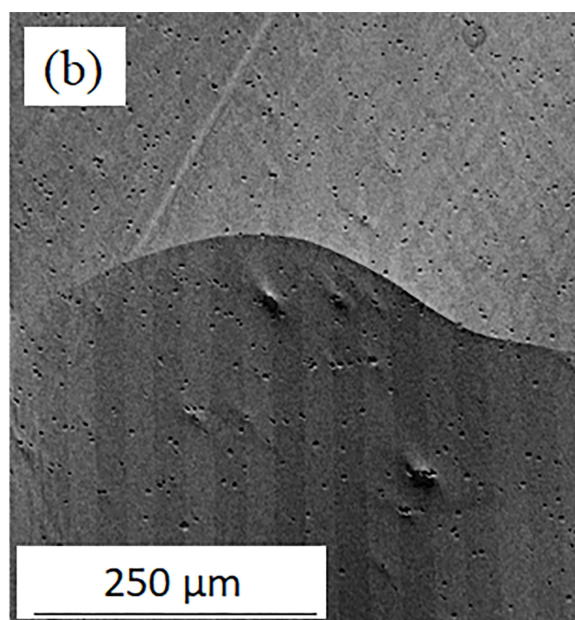
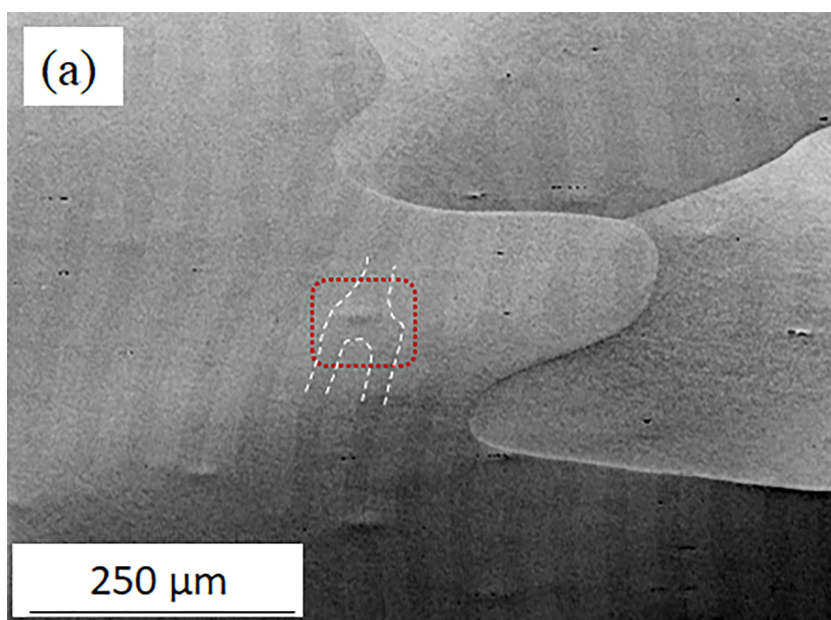
Table 4: Grain boundary angles and types in Samples A, B and C.

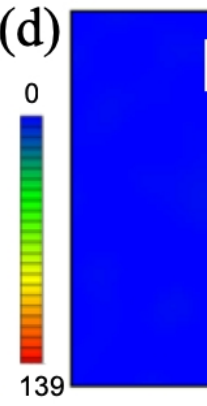
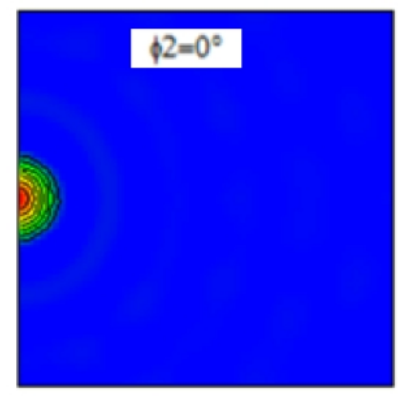
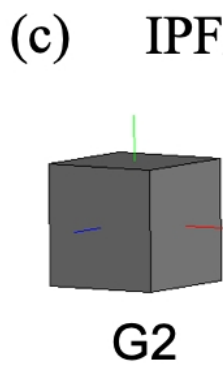
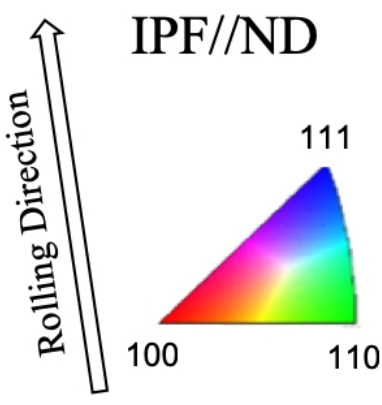
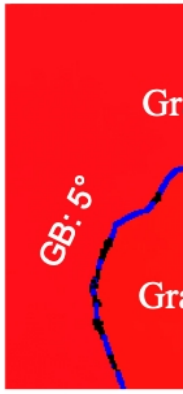
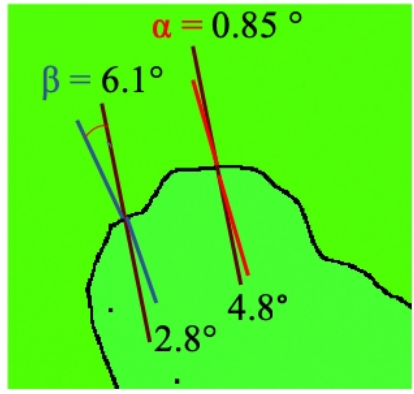
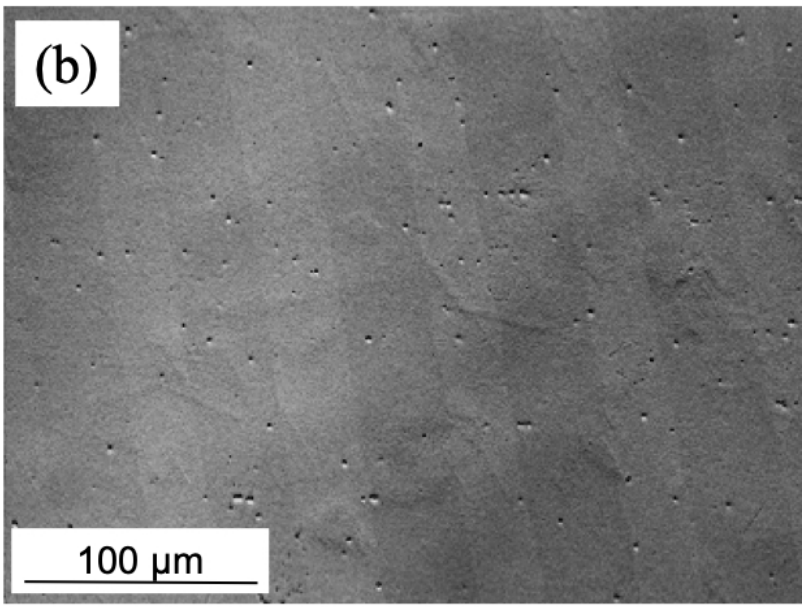
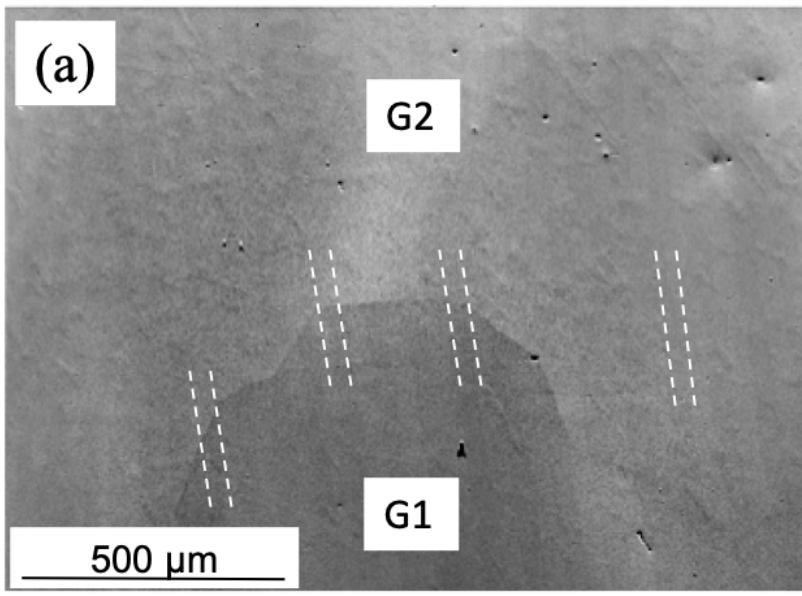
(a)

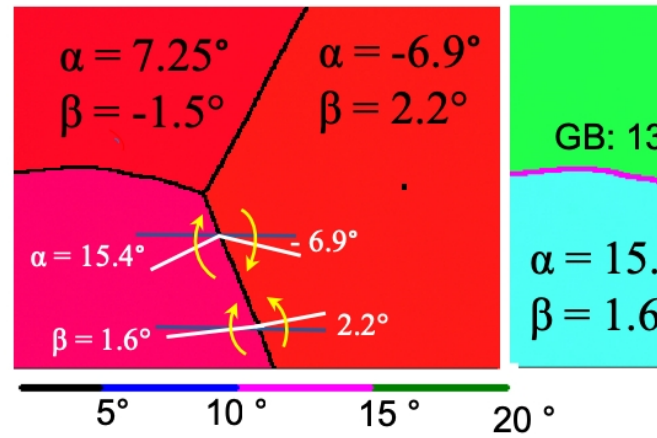
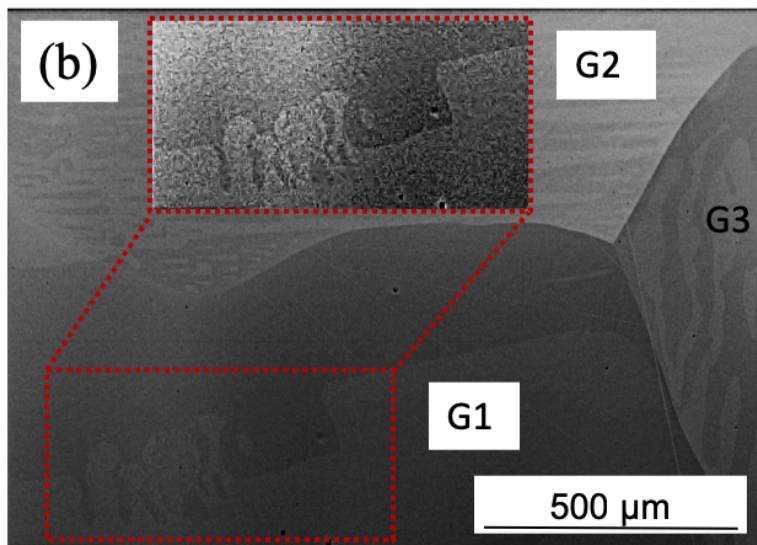
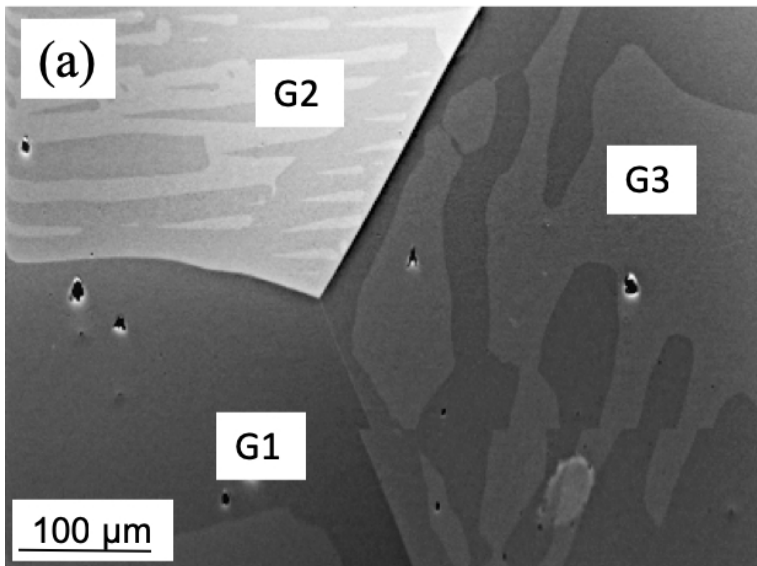


(b)



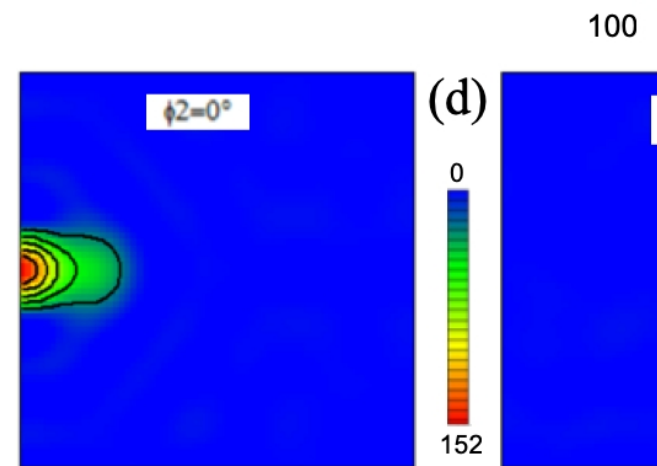
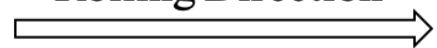


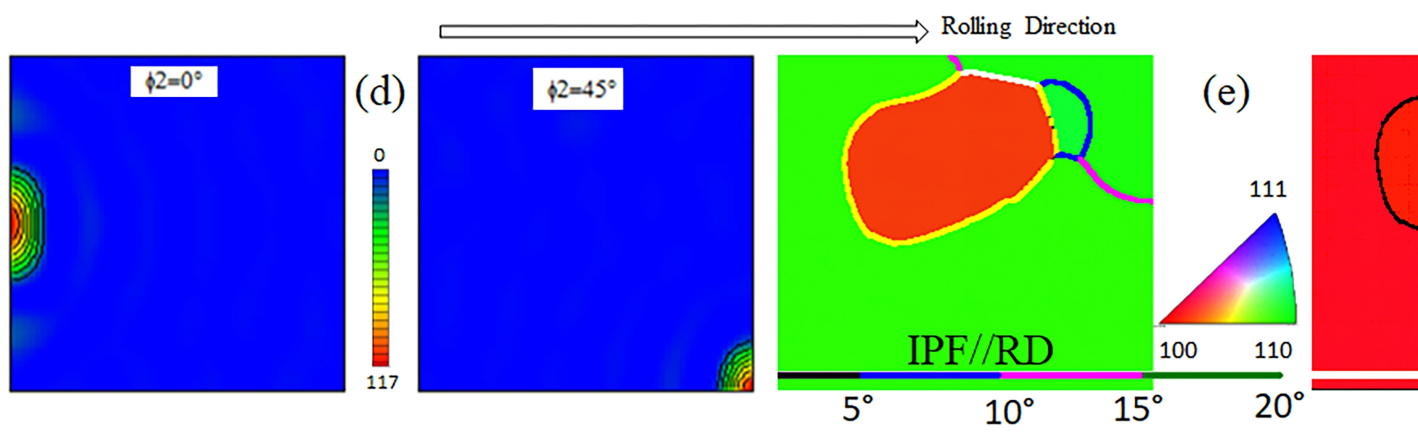
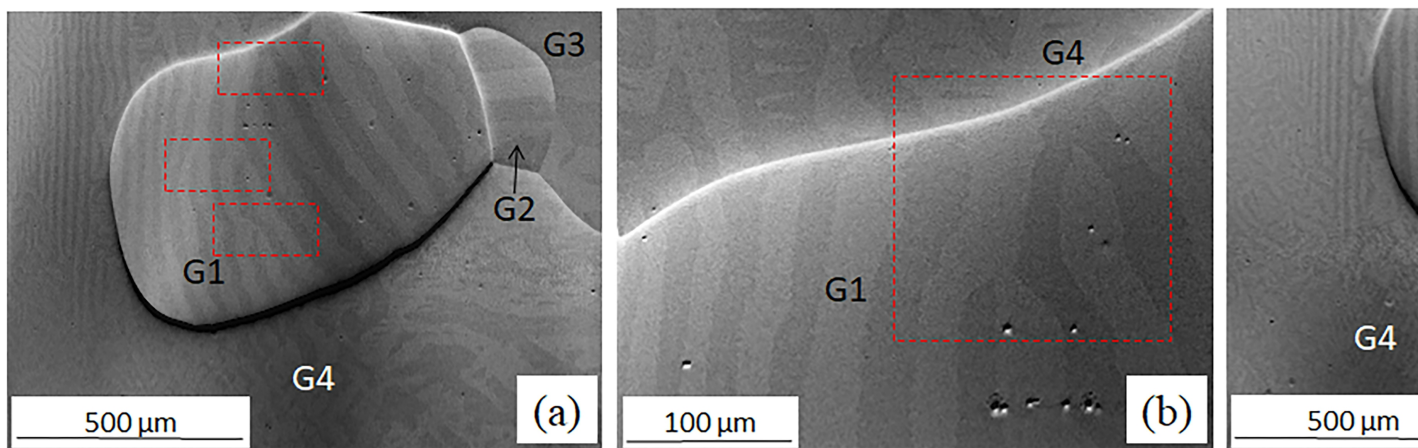


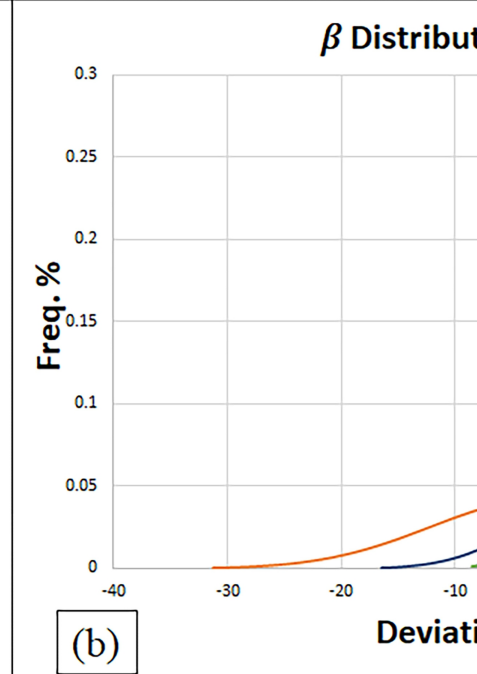
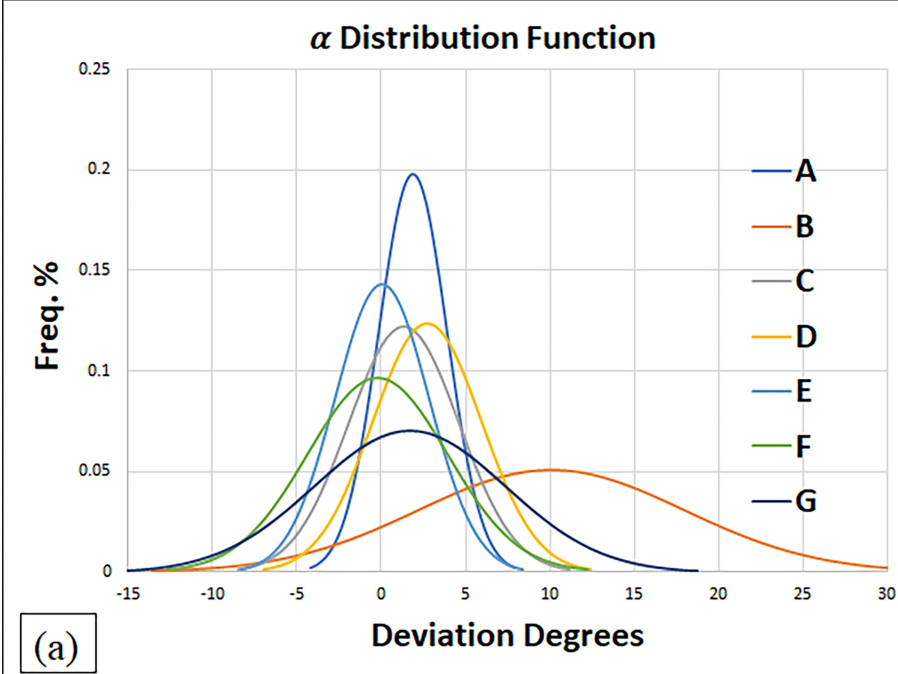


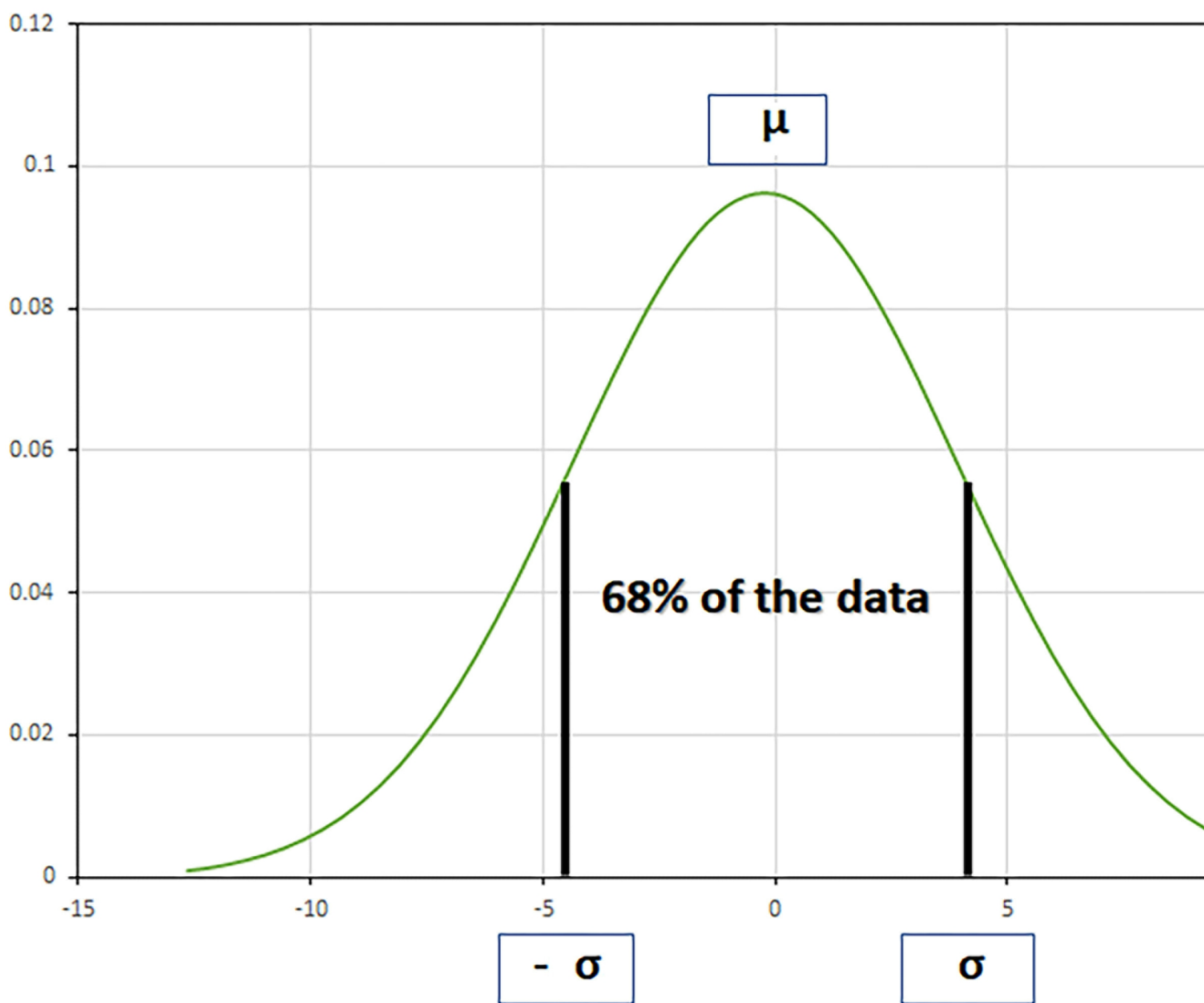
IPF//RD (c) IPF//RD

Rolling Direction

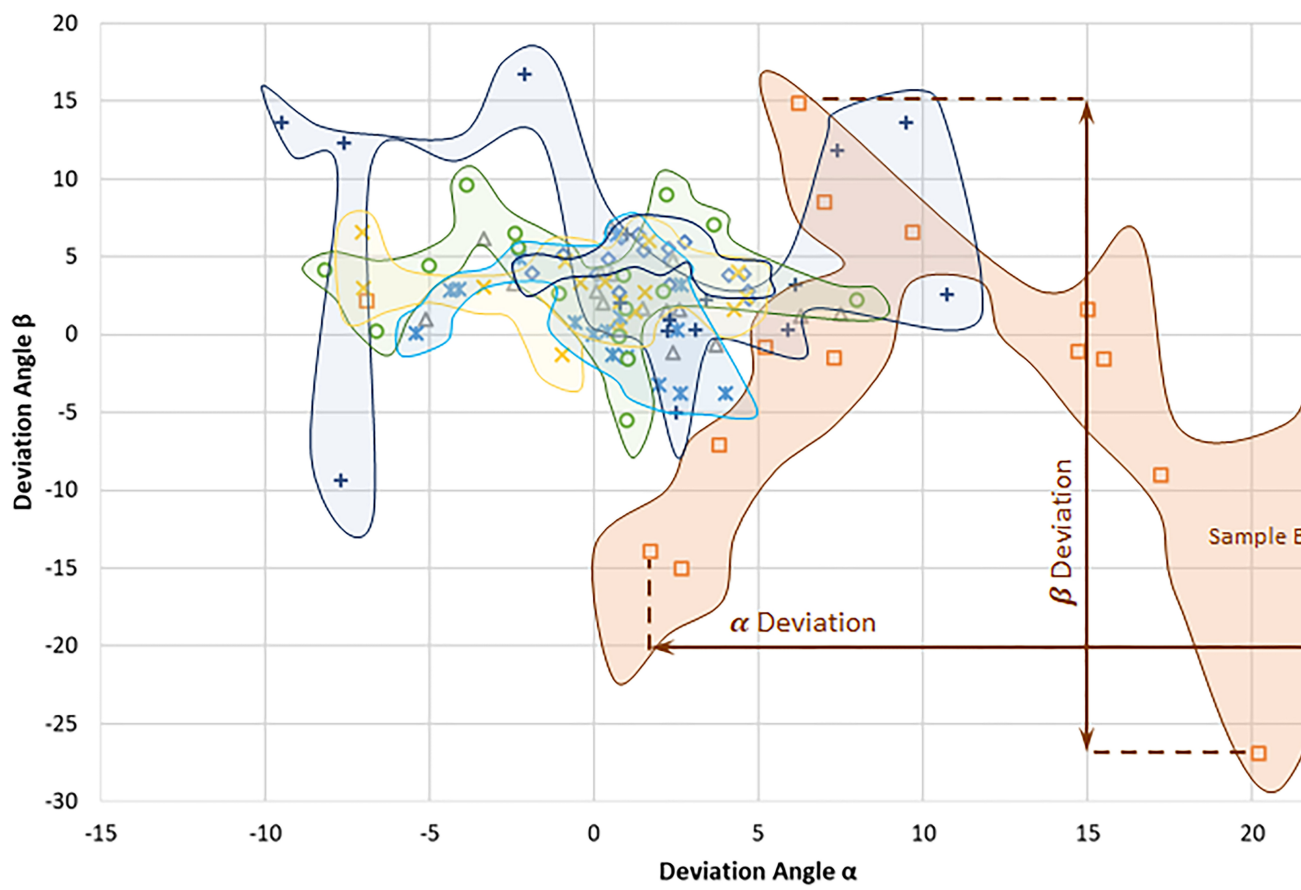


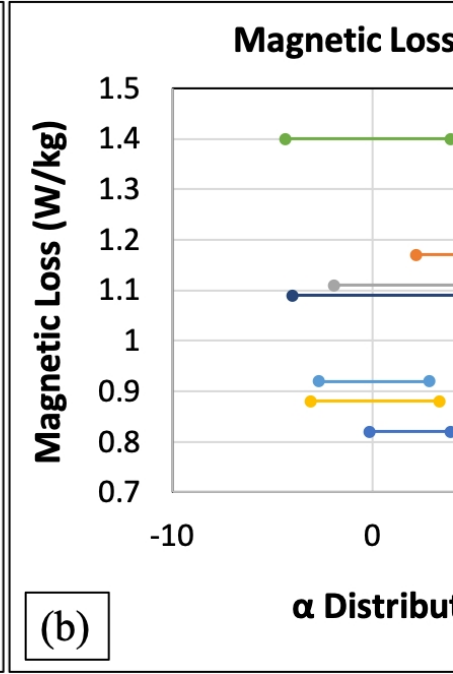
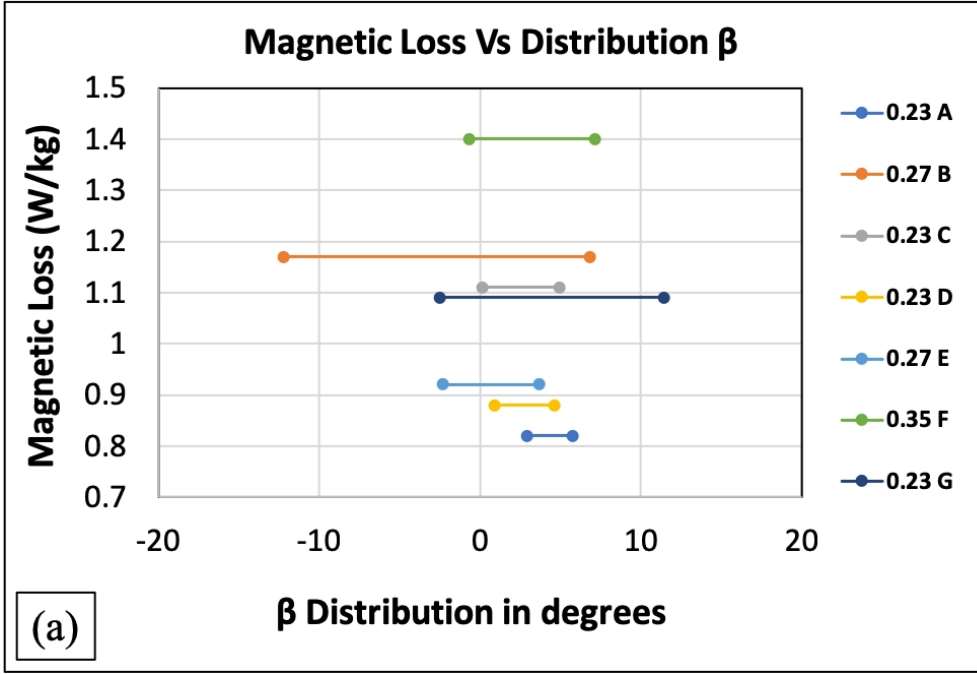


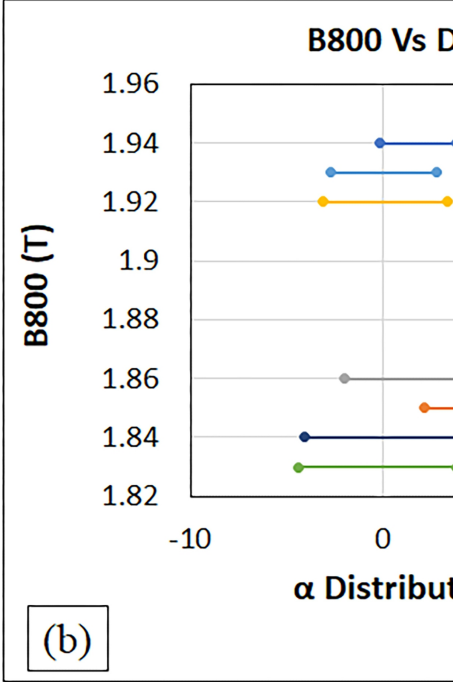
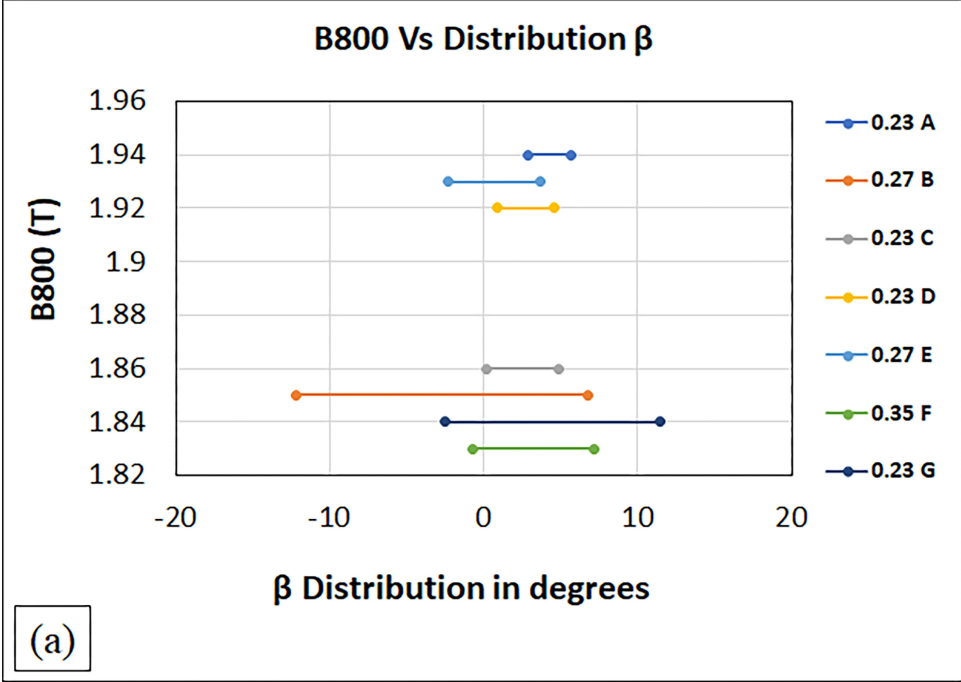


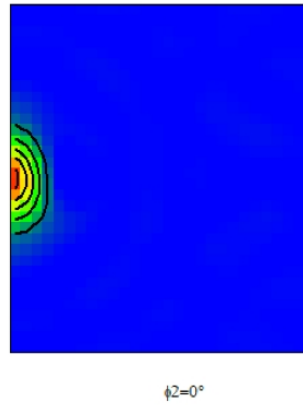
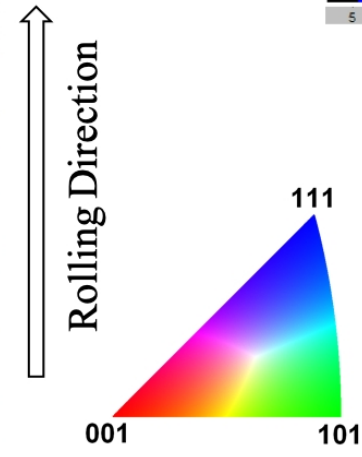
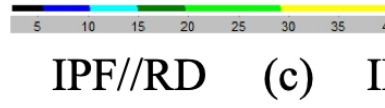
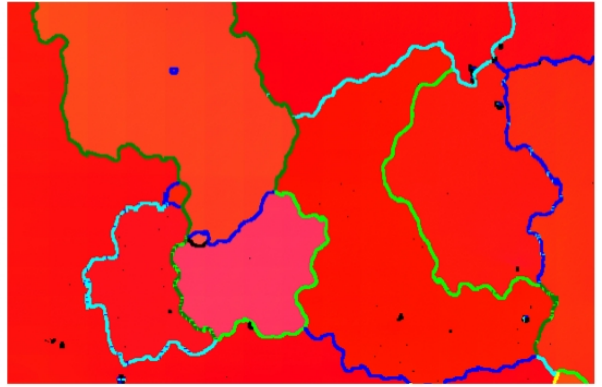
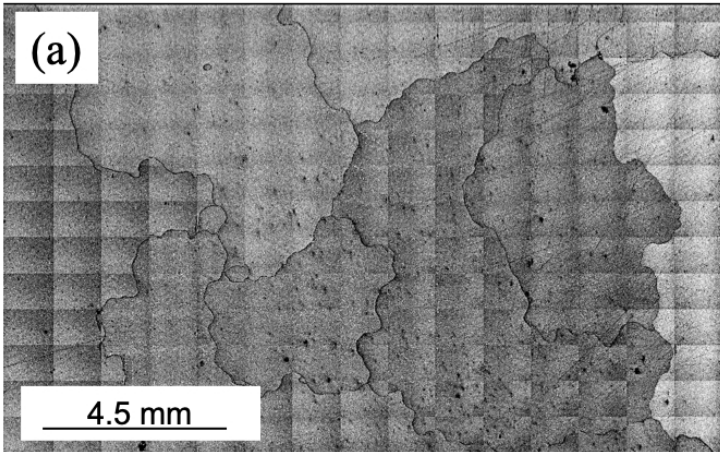


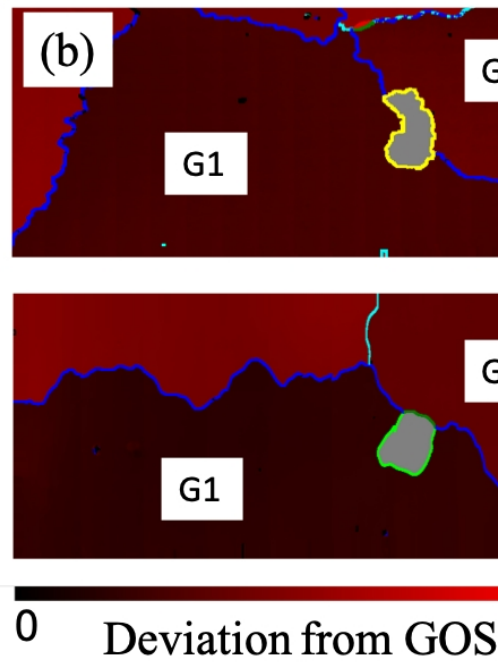
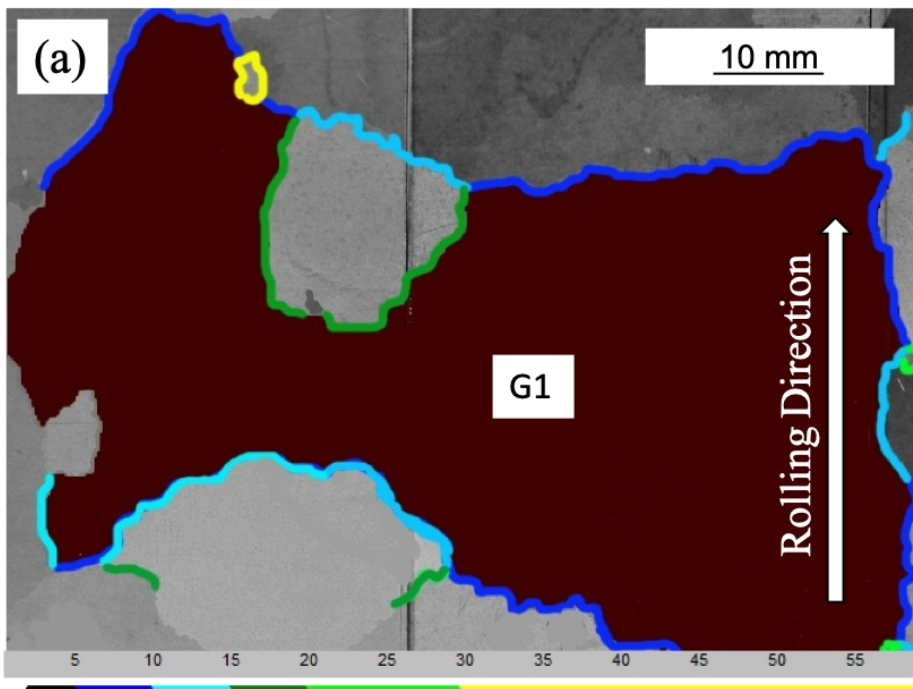
Deviation angles











<b>Sample</b>	<b>Magnetic losses (W/kg)</b>	<b>B800 (T)</b>	<b>T</b>
<b>A</b>	0.82	1.94	
<b>B</b>	1.17	1.85	
<b>C</b>	1.11	1.86	
<b>D</b>	0.88	1.92	
<b>E</b>	0.92	1.93	
<b>F</b>	1.4	1.83	
<b>G</b>	1.09	1.84	

<b>Voltage (keV)</b>	<b>Angle of Incidence (°)</b>
6	10
4	10
2	8

<b>Grains</b>	<b>Grain Boundary Type</b>	<b>Misorienta</b>
<b>Sample A</b>		
<b>G1-G2</b>	LAGB	5
<b>Sample B</b>		
<b>G1-G2</b>	HAGB	1
<b>G1-G3</b>	HAGB	2
<b>G2-G3</b>	HAGB	1
<b>Sample C</b>		
<b>G1-G2</b>	HAGB	3
<b>G1-G3</b>	HAGB	2
<b>G1-G4</b>	HAGB	3
<b>G2-G3</b>	LAGB	8
<b>G2-G4</b>	LAGB	8
<b>G3-G4</b>	LAGB	1

<b>Sample</b>	<b>Si</b>	<b>C</b>	<b>N</b>	<b>Mn</b>	<b>P</b>	<b>Al</b>	<b>Cu</b>	<b>Ni</b>
<b>A</b>	3.32	0.0017	0.0011	0.089	0.025	<0.005	0.006	<0.005
<b>B</b>	3.11	0.0026	<0.001	0.058	0.001	<0.005	0.12	0.062
<b>C</b>	3.33	0.0022	-	0.069	0.009	-	0.098	0.005
<b>D</b>	3.19	0.0025	<0.001	0.067	0.009	<0.005	0.063	0.031
<b>E</b>	3.19	0.0018	<0.001	0.065	0.009	<0.005	0.073	0.036
<b>F</b>	2.84	0.0016	<0.001	0.049	0.011	<0.005	0.15	0.057
<b>G</b>	3.23	0.0038	<0.001	0.059	0.003	<0.005	0.16	0.078